Temporally resolved single cell transcriptomics in a human model of amniogenesis

AUTHORS: Nikola Sekulovski[1,¶], Amber E. Carleton[1,¶], Anusha A. Rengarajan[1,¶], Chien-Wei Lin[2,¶], Lauren N. Juga[1], Allison E. Whorton[1], Jenna K. Schmidt[3], Thaddeus G. Golos[3,4,5], and Kenichiro Taniguchi[1,6,7,†]

AFFILIATIONS:

[1]Department of Cell Biology, Neurobiology and Anatomy, Medical College of Wisconsin, Milwaukee, WI 53226, USA

[2]Division of Biostatistics, Institute for Health and Equity, Medical College of Wisconsin, Milwaukee, WI 53226, USA

[3]Wisconsin National Primate Research Center (WNPRC), Madison, WI, USA

[4]Department of Obstetrics and Gynecology, University of Wisconsin - Madison School of Medicine, Madison, WI USA

[5]Department of Comparative Biosciences, University of Wisconsin - Madison School of Veterinary Medicine, Madison, WI, USA

[6]Department of Pediatrics, Medical College of Wisconsin, Milwaukee, WI 53226, USA

[7]Cancer Center, Medical College of Wisconsin, Milwaukee, WI 53226, USA

[¶]These authors contributed equally to this work

[†]Corresponding author

CONTACT:

Kenichiro Taniguchi

8701 Watertown Plank Road

B4245 BSB CB062

Milwaukee, WI 53226

ktaniguchi@mcw.edu

ABSTRACT

Amniogenesis is triggered in a collection of pluripotent epiblast cells as the human embryo implants. To gain insights into the critical but poorly understood transcriptional machinery governing amnion fate determination, we examined the evolving transcriptome of a developing human pluripotent stem cell-derived amnion model at the single cell level. This analysis revealed several continuous amniotic fate progressing states with state-specific markers, which include a previously unrecognized CLDN10^{+} amnion progenitor state. Strikingly, we found that expression of CLDN10 is restricted to the amnion-epiblast boundary region in the human post-implantation amniotic sac model as well as in a peri-gastrula cynomolgus macaque embryo, bolstering the growing notion that, at this stage, the amnion-epiblast boundary is a site of active amniogenesis. Bioinformatic analysis of published primate peri-gastrula single cell sequencing data further confirmed that CLDN10 is expressed in cells progressing to amnion. Additionally, our loss of function analysis shows that CLDN10 promotes amniotic but suppresses primordial germ cell-like fate. Overall, this study presents a comprehensive amniogenic single cell transcriptomic resource and identifies a previously unrecognized CLDN10^{+} amnion progenitor population at the amnion-epiblast boundary of the primate peri-gastrula.

INTRODUCTION

Amniogenesis is initiated during implantation in humans, and leads to the formation of an amniotic sac structure that surrounds and protects the developing embryo (Enders et al., 1983; Enders et al., 1986; Miki et al., 2005; Sasaki et al., 2016; Shahbazi and Zernicka-Goetz, 2018; Taniguchi et al., 2019). At implantation, the embryo (referred to at this time as a blastocyst) contains three morphologically and molecularly distinct cell types: 1) a collection of unpolarized pluripotent epiblast cells, precursors to both the embryo proper and the amniotic ectoderm, 2) a surrounding layer of polarized trophectoderm, a placental tissue precursor, and 3) an underlying extraembryonic primitive endoderm, a yolk sac precursor. Upon implantation, the pluripotent epiblast cells initiate epithelial polarization to form a cyst with a central lumen, the future amniotic cavity (Carleton et al., 2022; Shao and Fu, 2022). This event is followed by the fate transition of pluripotent epiblast cells that are in close proximity to the uterus to squamous amniotic ectoderm, forming a clear boundary between amnion and pluripotent epiblast territories of the cyst (Shahbazi and Zernicka-Goetz, 2018; Shao and Fu, 2022; Taniguchi et al., 2019). This asymmetric amnion-epiblast structure, known as the amniotic sac, provides the foundation for the next essential developmental steps (e.g., primitive streak formation, neural specification).

Recent studies using early human and monkey embryos have provided a basic understanding of the transcriptomic characteristics of early primate amniogenesis (Bergmann et al., 2022; Nakamura et al., 2016; Nakamura et al., 2017; Sasaki et al., 2016; Tyser et al., 2021; Yang et al., 2021). Yet, experimental dissection of the molecular mechanisms involved in this process is difficult in these *in vivo* models. To

enable molecular and cellular investigations, we and others developed human pluripotent stem cell (hPSC)-derived amnion models and showed that BMP signaling plays a crucial role in initiating amniogenesis (Chen et al., 2021; Overeem et al., 2023; Shao et al., 2017a; Shao et al., 2017b; Zheng et al., 2019). Recently, we further explored the BMP-dependent amniogenic transcriptional cascade, identifying several distinct transcriptional stages, as well as a requirement for TFAP2A-dependent transcription in regulating amnion fate progression (Sekulovski et al., 2024). However, changes in cellular differentiation states during amnion lineage progression remain largely unexplored.

In this study, we used single cell RNA sequencing (scRNA-seq) analysis to examine the dynamics in gene expression that accompany amnion differentiation of hPSC (herein referred to as the hPSC-amnion) cultured in a soft gel environment, called Gel-3D (Shao et al., 2017a). While no exogenous BMP is added in this Gel-3D amnion model, BMP signaling is activated in the cells by a mechanosensitive cue provided by the soft substrate, thereby initiating human amniogenesis (Shao and Fu, 2022; Shao et al., 2017a; Taniguchi et al., 2019). Interestingly, our data reveal contiguous amniogenic cell states: pluripotency-exiting, early progenitor, late progenitor, specified and maturing, each of which shows transcriptional similarities to distinct cell types in a Carnegie stage 7 human embryo (Tyser et al., 2021). Our data also reveal the presence of two non-amniotic cell types in the Gel-3D system: primordial germ cell-like and advanced mesoderm-like cells. Importantly, we identify a cohort of markers specific to each of these amnion lineage progressing states, and validate selected markers for their expression in the amnion from cynomolgus macaque (*Macaca fascicularis*) embryos.

Strikingly, we show that CLDN10, a marker of the progenitor population, exhibits a restricted amniotic expression pattern at the boundary between the amnion and the epiblast of the cynomolgus macaque peri-gastrula. This further supports our findings from a separate study (Sekulovski et al., 2024), which show that the amnion-epiblast boundary is a site of active amniogenesis in the macaque peri-gastrula. Furthermore, loss of CLDN10 results in the formation of primordial germ cell-like cells at the expense of amnion cells. Together, this study provides important single cell-level insight into human amnion fate progression and presents additional evidence for the presence of amnion progenitor cells in primate embryos undergoing gastrulation.

RESULTS

Previously, we described culture conditions (Gel-3D) in which plated hPSC form polarized cysts initially composed of columnar pluripotent cells, which then spontaneously undergo squamous morphogenesis and begin to express amnion markers (Shao et al., 2017a). Specifically, singly dissociated hPSC are plated densely on a soft gel substrate to form aggregates and are allowed to grow for 24 hours (hrs) in the presence of a ROCK inhibitor (Y-27632). After the first 24 hrs (day 1, d1), the ROCK inhibitor is removed (a trigger to initiate lumenal cyst formation (Hamed et al., 2023; Shao et al., 2017a; Taniguchi et al., 2015)), and a diluted extracellular matrix gel overlay (2% v/v, e.g., Geltrex) is added to provide an additional 3D cue. Immunofluorescent (IF) staining at this time shows cuboidal cells surrounding a central lumen; these cells express NANOG, but not TFAP2A (**Fig. 1A**).

116 Interestingly, 24 hrs after adding the gel overlay (d2), a subset of cells within the
117 cysts displays reduced expression of NANOG, while TFAP2A expression becomes
118 weakly activated (**Fig. 1A**, arrowhead in d2). By d3, NANOG is no longer detectable.
119 Moreover, while many cells exhibit prominent TFAP2A expression, some cells are only
120 weakly positive for TFAP2A (**Fig. 1A**, arrowheads). This pattern of TFAP2A expression
121 is consistent with the previous observation that amniogenesis initiates focally on the
122 pluripotent cysts and then spreads laterally to form fully squamous cysts (**Fig. 1A**,
123 (Sekulovski et al., 2024; Shao et al., 2017a; Shao et al., 2017b)). These molecular
124 changes are accompanied by a decrease in nuclear aspect ratio (a measure of
125 epithelial cell morphology) over time, revealing more flattened (squamous) shapes by
126 d3 and d4 (**Fig. 1B**, quantitation strategy shown in **Fig. S1A**, and previously established
127 in Shao et al., 2017a; Townshend et al., 2020)). These results provide further molecular
128 and structural evidence that the transition from pluripotent to amnion cell types occurs
129 progressively over the cyst, starting from focal initiation sites.
130 To explore transcriptional programs of the fate transitioning cells during early
131 stages of human amnion development in this model, we performed time-course scRNA-
132 seq analysis of developing hPSC-amnion cysts, harvested at d1, d2, d3 and d4. hPSC-
133 amnion cysts were dissociated into single cells, followed by single cell isolation and
134 labeling using the 10x Genomics Chromium system, cDNA amplification and
135 sequencing followed by demultiplexing (see Material and Methods for additional details).
136 This scRNA-seq dataset was examined using Seurat (Butler et al., 2018) for data
137 filtering, regression for genes associated with cell cycle progression, normalization,
138 variable gene selection and subsequent unsupervised clustering of cells (see Materials

139 and Methods). The data yield seven distinct populations among 8,765 cells (d1 = 1,359
140 (salmon), d2 = 1,546 (sage), d3 = 2,352 (light blue), d4 = 3,508 cells (purple), **Fig. 1C**),
141 which, after marker and lineage analyses described below, are labeled pluripotency-
142 exiting (salmon color, 1,363 cells), early progenitor (brown, 479 cells), late progenitor
143 (sage, 1,045 cells), specified (green, 1,366 cells) and maturing (purple, 2,795 cells),
144 PGC-LC (primordial germ cell-like cells, blue, 1,055 cells) and advM-LC (advanced
145 mesoderm-like cells, magenta, 662, **Fig. 1D**). Transcriptomic features of these cells are
146 visualized in Uniform Manifold Approximation and Projection (UMAP) plots (**Fig. 1C,D**).
147 To broadly characterize the transcriptional state of each population, we examined
148 the expression of known amnion markers (Roost et al., 2015; Shao et al., 2017a; Yang
149 et al., 2021; Zhao et al., 2024; Zheng et al., 2022). Consistent with the amniotic lineage,
150 early amnion markers (*ID2*, *GATA3* and *TFAP2A*, **Fig. 1E**, expression superimposed on
151 the UMAP plot in **Fig. 1C**) are widely expressed starting at d1 in pluripotency-exiting
152 cells that also show broad expression of pluripotency markers (**Fig. S1B**), while
153 intermediate markers that label specified amnion (*ISL1*, *HAND1*, *DLX5*, (Sekulovski et
154 al., 2024; Yang et al., 2021; Zhao et al., 2024)) show abundant expression by d3 (**Fig.
155 1F**). Late amnion genes such as *GABRP*, *VTCN*1 and *IGFBP3* (expressed in the first-
156 trimester human amnion (Roost et al., 2015) and also in other human amnion models
157 (Sekulovski et al., 2024; Shao et al., 2017a; Yang et al., 2021; Zhao et al., 2024; Zheng
158 et al., 2022)) are primarily enriched in the d3 and d4 populations (**Fig. 1G**). Interestingly,
159 most of the d2 cells show the expression of early, but not specified or pluripotency
160 (SOX2, NANOG), genes, suggesting that the d2 cell population may contain
161 transitioning cell types that give rise to specified amnion (brown and sage cells in **Fig.**

162 **1D**). Next, RNA-velocity analysis (Bergen et al., 2020) was applied to examine lineage
163 relationships based on the relative abundance of unspliced and spliced mRNA in each
164 cell. Indeed, the majority of the RNA-vector trajectories are directed from the cells in the
165 early progenitor (brown), late progenitor (sage), to specified (green) states (**Fig. 1H**).
166 In a recent study, we performed a detailed meta-analysis of the Tyser *et al.*
167 scRNA-seq dataset from a human embryo staged at Carnegie stage 7 (CS7) (Tyser et
168 al., 2021) and showed that the rod-shaped cluster of cells annotated as "Ectoderm" is
169 comprised of lineage progressing, lineage committed, and fully differentiated amnion
170 cell types (Sekulovski et al., 2024). The Tyser *et al*. UMAP plot is reproduced in **Fig.**
171 **S1C** with the original coordinates and annotations (expression of late markers, *GABRP*,
172 *VTCN*1 and *IGFBP3*, found at the distal tip of the rod-shaped "Ectoderm" population,
173 **Fig. S1C-E**). To examine which cells in the CS7 human embryo share transcriptomic
174 similarities to amnion progressing cells in Gel-3D, the scRNA-seq datasets from the
175 Tyser *et al.* CS7 human embryo and our d1-d4 Gel-3D time-course samples were
176 combined and normalized using an integration feature based on canonical correlation
177 analysis in Seurat (Hao et al., 2021) (**Fig. 1I-K**). Although the combined UMAP plot of
178 this integrated dataset shows some changes in shape from our original UMAP, it is clear
179 that "Epiblast", "Primitive Streak" and "Ectoderm" populations in the Tyser *et al.* dataset
180 closely map to the amnion progressing populations in our time-course Gel-3D dataset
181 (**Fig. 1I**, see **Fig. S1F** for mapping of each population). Indeed, the amniotic Tyser
182 "Ectoderm" cells primarily overlap with Gel-3D "specified" and "maturing" cell
183 populations, consistent with their amniotic fate; most Tyser "Epiblast" cells are seen in
184 the "pluripotency-exiting" population (**Fig. 1J,K**, **Fig. S1F**). Interestingly, Tyser "Primitive

185 Streak" cells are populated across several Gel-3D amniogenic cell states (**Fig. 1J,K**,
186 **Fig. S1F**), overlapping with the early (brown) and late (sage) progenitor populations,
187 suggesting that some Tyser "Primitive Streak" cells may be actively transitioning, and
188 that our early and late progenitor cells may display transcriptomic characteristics of fate
189 transitioning cells in human peri-gastrula.

190 Additionally, we identify two non-amniotic cell types that show transcriptional
191 characteristics of PGC- (blue) and advM- (magenta) like cells (**Fig. 1D**). The Tyser-Gel-
192 3D integration analysis shows that the blue cells overlap with the Tyser "Primitive
193 Streak" cells that abundantly express PGC markers (e.g., *PRDM1*, *SOX17*, *NANOS3*,
194 *PRDM14*, *NANOG*, *XACT*, **Fig. 1L**). Several Tyser "Advanced Mesoderm" cells are
195 seen in the magenta cells, and our marker analysis shows that developed mesoderm
196 makers (*HAND2*, *GATA4*, *PITX2*, *ISL1*, *HAND1*) are enriched (**Fig. 1M**, summary of
197 additional markers found in **Fig. 1N**). Strikingly, the RNA velocity trajectories are
198 directed from the interface of the early/late amnion progenitor populations to the PGC-
199 LC (**Fig. 1H**), suggesting their close transcriptomic characteristics. These findings
200 support a growing notion that amnion and PGC progressing cells initially share a
201 common intermediate lineage (Castillo-Venzor et al., 2023; Chen et al., 2019; Xiao et
202 al., 2024; Zheng et al., 2022). The advM-LC population may have formed due to high
203 BMP signaling (Schultheiss et al., 1997; Tsaytler et al., 2023; van Wijk et al., 2007).

204 To identify genes that are unique to each cluster, unsupervised differential gene
205 enrichment analysis was performed (**Table 1**, adjusted p-value < 0.05). As expected,
206 pluripotency markers are seen in the pluripotency-exiting cluster, and the specified and
207 maturing clusters show enriched expression of known late amnion markers as well as

208 previously uncharacterized genes (*ADAMTS18*, *SESN3* (**Fig. 1N**) – RNA *in situ*
209 hybridization in a cynomolgus macaque (*Macaca fascicularis*) embryo staged between
210 CS12 and CS13, an organogenesis stage, shown in **Fig. S2A-C**).
211 The most differentially expressed genes in early (brown) and late (sage)
212 progenitor populations are *TBXT* (T-box transcription factor T) and *CLDN10* (a gene
213 encoding Claudin-10, a component of the tight junction), respectively (**Fig. 2A,B**, top
214 three genes plotted in **Fig. 2C**). Recently, we showed that amnion lineage progression
215 in Glass-3D^{+BMP}, another model of human amniogenesis, traverses an intermediate
216 transcriptional phase weakly expressing *TBXT* (*TBXT*^{low}) before specified markers (e.g.,
217 *ISL1*, *HAND1*, *DLX5*) are expressed, revealing lineage progressing characteristics of
218 the cells in the *TBXT*^{low} transcriptional phase (Sekulovski et al., 2024). The same study
219 also showed that cells displaying transcriptomic characteristics consistent with fate
220 progression from *TBXT*^{low} to *ISL1*$^{+}$/*HAND1*$^{+}$ specified state are also seen in the Tyser *et*
221 *al.* CS7 human embryo as well in the Yang *et al.* d14 cynomolgus macaque embryo
222 datasets (Sekulovski et al., 2024). In Gel-3D, while most cells in the early progenitor
223 population express some level of *TBXT*, only a few cells express abundant *TBXT* (**Fig.**
224 **2A**). Indeed, our IF time-course analysis shows that cells with weak TBXT expression
225 are seen at d2 in several cells that are not yet expressing ISL1 (**Fig. 2D**, arrowheads);
226 TBXT expression is largely missing in d3 and d4 cysts (**Fig. 2D**), confirming the
227 presence of an early and transient *TBXT*^{low} state in developing Gel-3D hPSC-amnion
228 cysts.
229 Prominent *CLDN10* expression is seen throughout the late progenitor population
230 (*CLDN10*^{high}), but is rapidly diminished in the specified cells (**Fig. 2B**). Although at lower

levels, some *CLDN10* expression is observed in the pluripotency-exiting and early progenitor states (*CLDN10*^{low}, **Fig. 2B,C**), consistent with our previous bulk-RNA sequencing analysis showing that low *CLDN10* expression is seen in pluripotent cells (Shao et al., 2017a). Using IF staining in Gel-3D hPSC-amnion model, we validated a dynamic expression pattern of CLDN10 over time (**Fig. 2D,E**). Despite broadly expressed at transcript levels in hPSC-amnion cysts at d2 (**Fig. 2B**), CLDN10 expression is seen in the small fraction of cells that are weakly positive for TBXT and TFAP2A (**Fig. 2D,E**, arrowheads, quantitation in **Fig. 2F**). At d3, CLDN10 is co-expressed with TFAP2A in several, but not all cells (**Fig. 2E**). Further, ISL1^{high} cells do not show clear CLDN10 membrane staining (**Fig. 2D**). In contrast, most cells at d4 retain abundant TFAP2A and ISL1 expression but do not express CLDN10 (**Fig. 2D,E**). Importantly, our analysis for nuclear aspect ratio (NAR) shows that, at d2, CLDN10^{+} cells (mean NAR = 0.54 $\pm$ 0.17 STDEV, n = 39) are significantly more squamous compared to CLDN10^{-} cells (NAR = 0.97 $\pm$ 0.31 STDEV, n = 87, $p<0.001$). While previous studies implicated *CLDN10* as an amnion marker (Zheng et al., 2019; Zheng et al., 2022), a detailed analysis was not performed. Thus, these data present evidence suggesting that CLDN10^{high} marks a later transient progenitor state that follows an earlier *TBXT*^{low}/*CLDN10*^{low} progenitor state, but CLDN10 expression is extinguished in more differentiated cells. Single cell transcriptomic characteristics consistent with this lineage progression from the *TBXT*^{low}/*CLDN10*^{low} state to the *CLDN10*^{high} state is also seen in the Tyser *et al.* CS7 human embryo as well in the Yang *et al.* d14 cynomolgus macaque embryo datasets (**Fig. S3A-C**).

253 Interestingly, in PASE (post-implantation amniotic sac embryoids), an *in vitro*
254 model of human amniotic sac formation (Shao et al., 2017b), CLDN10 is localized
255 specifically to cells at the boundary between squamous amnion and columnar
256 pluripotent cells (**Fig. 3A** , arrowheads). To test whether CLDN10^{+} progenitor-like
257 boundary cells are present in the developing primate amniotic sac *in vivo*, we analyzed
258 CLDN10 expression in a cynomolgus macaque embryo displaying the amniotic sac
259 (**Fig. 3B**, staged between CS6 and CS7). Strikingly, CLDN10 expression is exclusively
260 seen at the boundary separating amnion and epiblast tissues. These results are
261 consistent with our recent findings indicating that this boundary is likely a site of active
262 amniogenesis (i.e., epiblast cells at the boundary actively undergo amnion specification)
263 in the primate peri-gastrula (Sekulovski et al., 2024). Importantly, a cynomolgus
264 macaque embryo from a later stage (**Fig. 3C,D**, CS10) also shows CLDN10 positive
265 cells at the amnion-embryo boundary. In the CS10 embryo, while a collection of cells
266 expressing weak CLDN10 is seen posteriorly (**Fig. 3C,D** – inset (iii)), CLDN10
267 expression is highly prominent anteriorly in the cells at the boundary of the amnion and
268 the developing mediolateral placode (**Fig. 3C,D** – inset (i), additional images in **Fig.**
269 **S3D,E**). Together, these results establish the presence of previously unrecognized
270 CLDN10^{+} amnion-embryo boundary population that primarily gives rise to amnion
271 during gastrulation as well as during early organogenesis in the cynomolgus macaque.
272 To investigate the role of CLDN10, H9 hESC lacking CLDN10 were cultured in
273 the Gel-3D condition (**Fig. 4A-D**, see **Fig. S4** for generation of *CLDN10*-KO lines).
274 Morphologically, while *CLDN10*-KO cyst formation is largely similar to controls by d3, by
275 d4, squamous morphogenesis as well as overall cyst formation are disrupted.

276 Interestingly, our IF analysis shows that, in the KO background, SOX2 expression
277 gradually reduces overtime similar to controls, but cells expressing ISL1 are reduced by
278 d4 (**Fig. 4A,B**). Given the presence of PGC-LC in Gel-3D (**Fig. 1D,L**), we next
279 examined the expression of PGC markers. Strikingly, while very few cells are
280 NANOG^{+}/SOX17^{+} PGC-LC in controls at d4, NANOG/SOX17 double positive cells are
281 seen prematurely at d2 as well as at d3 (**Fig. 4C,D**). These results suggest that
282 CLDN10 functions to promote amnion fate progression, and prevent emergence of the
283 PGC-like lineage.
284

285 **DISCUSSION**

286 Together, this study presents a temporally resolved single cell transcriptomic resource
287 for future investigations of the amniogenic transcriptional cascade in developing primate
288 embryos. In summary, we have profiled the transcriptomic signatures of lineage
289 progressing cells in an *in vitro* model of hPSC-amnion development, and identified 1)
290 five contiguous amnion progressing states (outlined in **Fig. 4E**) including two previously
291 unrecognized amnion progenitor populations, 2) an amnion progenitor population
292 labeled by CLDN10 at the boundary between the amnion and the epiblast of the primate
293 amniotic sac (model schematic in **Fig. 4F**), and 3) the role of CLDN10 in maintaining
294 amnion fate progression.

295 Our time-course scRNA-seq analysis showed that PGC-LC are present in our
296 Gel-3D model, and that some of the amnion progenitor population may contribute to
297 PGC-LC, supporting a growing notion that amnion and PGC progressing cells initially
298 share a common lineage (Castillo-Venzor et al., 2023; Chen et al., 2019; Xiao et al.,

299 2024; Zheng et al., 2022), and providing detailed transcriptomic insights into this lineage
300 diversification step that occurs in the Gel-3D system (**Fig. 4E**). Moreover, the loss of
301 CLDN10, a marker of the late amnion progenitor and a tight junction component, leads
302 to increased PGC-LC formation, while amnion formation is reduced. Interestingly, a
303 recent study by Vasic *et al.* showed that reduced level of TJP1 (also known as ZO-1) in
304 unconfined hPSC monolayer colonies treated with BMP4 (a system that undergoes
305 gastrulation-like patterning (Joy et al., 2021) similar to the micropatterned gastruloid
306 model, (Heemskerk et al., 2017; Warmflash et al., 2014) leads to increased emergence
307 of a germ cell lineage (Vasic et al., 2023). Therefore, our results present additional
308 evidence for the role of tight junction formation in suppressing PGC lineages, and
309 demonstrate a key role of CLDN10 in maintaining amnion fate progression in progenitor
310 cells. Given that Claudin proteins control tight junction properties and epithelial
311 characteristics (Angelow et al., 2008), CLDN10 might also be critical for organizing a
312 boundary structure containing shape/fate-transitioning cells flanked by squamous
313 amnion or columnar/pseudostratified pluripotent cells on each side.

314 Previous studies established that BMP is a major trigger of amniogenesis. What
315 other potential mechanisms could help to initially induce and maintain the half amnion-
316 half epiblast structure? Trophectoderm may play some roles in triggering amnion
317 specification given that these cells directly overlay the nascent amnion during
318 implantation. Indeed, molecular characterization of early cynomolgus macaque embryos
319 by Sasaki *et al.* (Sasaki et al., 2016) have suggested that the trophectoderm may
320 provide some cue (e.g., secreted ligands) to the underlying epiblast cells. Also, a recent

321 study by Pedroza *et al.* showed that co-culturing hPSC on a monolayer of human
322 trophoblast stem cells helps initiate amniogenesis (Pedroza et al., 2023).
323 Furthermore, visceral endoderm might play an important role in defining the zone
324 in which amniogenesis can occur, helping to shape the amnion-epiblast boundary
325 territory. Studies have established that visceral endoderm plays a major role in embryo
326 patterning by expressing secreted BMP antagonists (Chambers et al., 2009; Perea-
327 Gomez et al., 2002; Shawlot et al., 1999), even at very early stages of implantation
328 (Bergmann et al., 2022; Sasaki et al., 2016). Therefore, it is possible that, during
329 implantation, epiblast cells that are in close proximity to visceral endoderm contribute to
330 embryo proper because the presence of secreted BMP antagonists prevents them from
331 undergoing amniogenesis. However, more distal epiblast cells at the uterine-proximal
332 pole of the epiblast cyst, which are farther away from the BMP antagonist source, can
333 respond to BMP signaling and form amnion. The amnion-epiblast boundary territory
334 might be the most distal region at which amniogenesis can take place, and the balance
335 between the rate of epiblast proliferation and the rate of amniogenesis at the boundary
336 likely contributes to maintaining the ratio between amnion and epiblast cells in
337 implanting embryos, as well as in peri-gastrula.
338 Recently, single cell transcriptomics analysis has emerged as a valuable tool to
339 ground findings from *in vitro* models with natural as well as cultured primate embryo
340 systems (e.g., (Yang et al., 2021; Zhao et al., 2024; Zheng et al., 2022)). To aid in
341 additional investigations, several culture systems have been developed to generate
342 amnion, and single cell transcriptomic analyses have been performed in several of the
343 systems (e.g., (Chen et al., 2019; Minn et al., 2020; Overeem et al., 2023; Rostovskaya

344 et al., 2022)). Future transcriptomic comparisons of the amnion in each of these models
345 will enable us to gain additional insights into amniogenic mechanisms.
346

347 **MATERIALS AND METHODS**

348 *hESC lines*

349 Human embryonic stem cell line H9 was used in this study (WA09, P30, P48, WiCell;
350 NIH registration number: 0062). All protocols for the use of hPSC lines were approved
351 by the Human Stem Cell Research Oversight Committee at the Medical College of
352 Wisconsin and the Human Pluripotent Stem Cell Research Oversight Committee at the
353 University of Michigan. All hPSC lines were maintained in a feeder-free system for at
354 least 20 passages and authenticated as karyotypically normal at the indicated passage
355 number. Karyotype analysis was performed at Cell Line Genetics. All hPSC lines tested
356 negative for mycoplasma contamination (LookOut Mycoplasma PCR Detection Kit,
357 Sigma-Aldrich). In summary, hESC were maintained in a feeder-free culture system with
358 mTeSR1 medium, or with 50%/50% mix of mTeSR1 and mTeSR plus (STEMCELL
359 Technologies). hESC were cultured on 1% (v/v) Geltrex (Thermo Fisher Scientific), or
360 with Cultrex SCQ (Bio-techne) coated 6 well plates (Nunc). Cells were passaged as
361 small clumps every 4 to 5 days with Dispase (Gibco). All cells were cultured at 37°C
362 with 5% CO_2. Media was changed every day. hESC were visually checked every day to
363 ensure the absence of spontaneously differentiated, mesenchyme-like cells in the
364 culture. Minor differentiated cells were scratched off the plate under a dissecting scope
365 once identified. The quality of all hESC lines was periodically examined by
366 immunostaining for pluripotency markers and successful differentiation to three germ

367 layer cells. Similar methods were previously used in (Sekulovski et al., 2024; Wang et
368 al., 2021).
369
370 *Gel-3D hPSC-amnion formation assays*
371 Methods for these assays have been previously described (Shao et al., 2017a; Shao et
372 al., 2017b) with exceptions that 60-70uL of undiluted ECM gel solution is hand-streaked
373 on ice cold 22mmx22mm square coverslips, and that, in addition to Geltrex (Life
374 Technologies), Cultrex Ultimatrix (Bio-Techne) was also used. Singly dissociated cells
375 were prepared using Accutase (Sigma-Aldrich) and were plated on ECM gel-coated
376 coverslips at 25,000 cells/cm^2 in mTeSR1 or in 50%/50% mTeSR1/mTeSR plus mix
377 medium in the presence of 10μM Y-27632 (STEMCELL Technologies). After 24 hr, cells
378 were then incubated in media containing 2% Geltrex/Ultimatrix overlay without Y-27632
379 with daily media changes (note that 1% gel overlay was used between d2 to d4).
380
381 *DNA constructs*
382 *piggyBac-CRISPR/Cas9 (pBACON) constructs*
383 A piggyBac-CRISPR/Cas9 (pBACON) vector that contains SpCas9-T2A-puro and hU6-
384 gRNA expression cassettes flanked by piggyBac transposon terminal repeat elements
385 (pBACON-puro), which allows subcloning of annealed oligos containing gRNA
386 sequence at *BbsI* site, has been previously described (Shao et al., 2017b; Townshend
387 et al., 2020; Wang et al., 2021). gRNA targeting genomic sites and oligo sequences to
388 generate pBACON-puro-h*CLDN10*-ICL1 (primers: CRISPR_hCLDN10ICL#1_s and
389 CRISPR_hCLDN10ICL#1_as) are found in **Fig. S4** and **Table 2**; these were designed

390 using a publicly available tool

391 (https://www.idtdna.com/site/order/designtool/index/CRISPR_CUSTOM). Similar

392 methods were previously used in several publications (e.g., (Sekulovski et al., 2024;

393 Wang et al., 2021)).

394

395 *piggyBac-based transgenic and genome edited hESC lines*

396 PB constructs (3μg) and pCAG-ePBase (Lacoste et al., 2009) (1μg) were co-transfected

397 into H9 hESC (70,000 cells cm^{-2}) using GeneJammer transfection reagent (Agilent

398 Technologies). To enrich for successfully transfected cells, drug selection (puromycin,

399 2μg/mL for 4 days) was performed 48- to 72-hrs after transfection. hESC stably

400 expressing each construct maintained the expression of pluripotency markers.

401 During pBACON-based genome editing, puro-selected cells were cultured at low

402 density (300 cells cm^{-2}) for clonal selection. Established colonies were manually picked

403 and expanded for screening indel mutations using PCR amplification of a region

404 spanning the targeted gRNA region (genomic DNA isolated using DirectPCR Lysis

405 Reagent (Tail) (VIAGEN), primers: hCLDN10, Geno_hCLDN10CDS2_RI_fw and

406 Geno_hCLDN10CDS2_NI_rv), which were subcloned into pPBCAG-GFP (Chen and

407 LoTurco, 2012) at EcoRI and NotI sites, and sequenced (Seq-3'TR-pPB-Fw). At least

408 12 to 15 bacterial colonies were sequenced (Sanger sequencing) to confirm genotypic

409 clonality. Control cells are wild-type, unedited H9 hESC in all loss-of-function

410 experiments.

411

412 *Cynomolgus macaque*

413 *Animals*

414 The female and male cynomolgus macaques were housed and cared for at the Wisconsin
415 National Primate Research Center (WNPRC). All procedures were performed in
416 accordance with the NIH Guide for the Care and Use of Laboratory Animals and under
417 approval of the University of Wisconsin College of Letters and Sciences and Vice
418 Chancellor Office for Research and Graduate Education Institutional Animal Care and
419 Use Committee (protocol g005061).

420

421 *Animal breeding and pregnancy detection*

422 Beginning on day 8 post-onset of menses, the female was housed with a compatible
423 male and monitored for breeding. Animals were pair-housed until day 16-20 post-onset
424 of menses. A 2-3 mL blood draw was performed daily from day 8 post-onset of menses
425 until day 16 to assess the timing of ovulation based on the estradiol peak and rise in
426 progesterone in serum. Serum samples were analyzed for estradiol (25 μL) and
427 progesterone (20 μL) using a cobas e411 analyzer equipped with
428 ElectroChemiLuminescence technology (Roche, Basal, Switzerland) according to
429 manufacturer instructions. Results were determined via a calibration curve which was
430 instrument-generated by 2-point calibration using traceable standards and a master
431 curve provided via the reagent barcode. Inter-assay coefficient of variation (CV) was
432 determined by assaying aliquots of a pool of rhesus plasma. For estradiol, the limit of
433 quantitation (LOQ) was 25 pg/mL, the intra-assay CV was 2.02%, and the inter-assay
434 CV was 5.05%. For progesterone, the LOQ was 0.2 ng/mL, the intra-assay CV was
435 1.37%, and the inter-assay CV was 4.63%. A transabdominal ultrasound was performed

436 to detect pregnancy as early as 14 days post-ovulation. The ultrasound measurements
437 in combination with the timing of ovulation were used to estimate the day of conception
438 and gestational age of the pregnancy.
439
440 *Terminal perfusion uterine collection, paraffin embedding, sectioning and staining*
441 The pregnant females were sedated with intramuscular ketamine (>15 mg/kg) followed
442 by IV sodium pentobarbital (>35 mg/kg) and then perfused with 4% paraformaldehyde
443 (PFA) via the left ventricle. The entire uterus and cervix were removed. The serosa and
444 superficial myometrium were scored for better fixative penetration and to denote dorsal
445 and ventral orientation. Tissues were fixed in 4% PFA with constant stirring and solution
446 changes were performed every 24 hrs for a total of 72 hrs. The uterus was serially
447 sectioned from the fundus to the internal cervical os into 4 mm slices using a dissection
448 box. Cassettes with tissue sections were transferred into 70% ethanol, routinely
449 processed in an automated tissue processor and embedded in paraffin for histological
450 analyses (5 μm sections). Fixed uterine tissue were cut in 5 μm thick cross-sections,
451 mounted on slides, deparaffinized in xylene and rehydrated in an ethanol series. Antigen
452 retrieval was performed by boiling in citrate buffer. Sections were blocked 4% goat serum
453 in PBS at RT for at least 3-hr. Subsequent immunolocalization was performed using
454 commercially available primary antibodies, incubated overnight at 4 °C in 4% serum.
455 Immunofluorescent detection was performed using secondary antibodies tagged with a
456 fluorescent dye (fluorophores excitation = 488, 555, and 647nm), and counterstained with
457 DAPI. Negative controls were performed in which the primary antibody was substituted

458 with the same concentration of normal IgG of the appropriate isotype. Images were
459 obtained with a Zeiss LSM980 microscope.
460 Note that similar methods were used in (Sekulovski et al., 2024).
461
462 *Confocal microscopy of fixed samples*
463 Confocal Images of fixed samples were acquired using a Nikon-A1 (Nikon) and a Zeiss
464 LS980 laser scanning confocal microscopes. Non-3D images were generated using
465 Zen, FIJI (NIH) and Photoshop (Adobe).
466
467 *Immunostaining*
468 hPSC-amnion cysts grown on the coverslip were rinsed with PBS (Gibco) twice, fixed
469 with 4% paraformaldehyde (Sigma) for 60 min, then rinsed with PBS three times, and
470 permeabilized with 0.1% SDS (Sigma, in 1x PBS) solution for 60 min. The samples
471 were blocked in 4% heat-inactivated goat serum (Gibco) or 4% normal donkey serum
472 (Gibco) in PBS overnight at 4°C. The samples were incubated with primary antibody
473 solution prepared in blocking solution at 4°C for 48 hr, washed three times with PBS (30
474 min each), and incubated in blocking solution with goat or donkey raised Alexa Fluor-
475 conjugated secondary antibodies (Thermo Fisher), at room temperature for 24 hours.
476 Counter staining was performed using Hoechst 33342 (nucleus, Thermo Fisher
477 Scientific), Alexa-Fluor-conjugated wheat germ agglutinin (membrane, Thermo Fisher
478 Scientific) and Phalloidin (F-ACTIN, Thermo Fisher). All samples were mounted on
479 slides using 90% glycerol (in 1x PBS). When mounting hPSC-cysts samples, modeling
480 clay was used as a spacer between coverslip and slide to preserve lumenal cyst

481 morphology. Antibodies for IF staining are found in **Table 2**. Similar staining method
482 was previously used in (Shao et al., 2017a; Shao et al., 2017b).
483
484 *RNA isolation and Single cell RNA sequencing*
485 Gel-3D hPSC-amnion samples were rinsed once with cold 1x PBS prior to treating with
486 Cultrex Organoid Harvesting solution (R&D Systems) to non-enzymatically
487 depolymerize Ultimatrix (gel bed, R&D systems), which were then dissociated into
488 single cell suspensions using the Neural Tissue Dissociation Kit (P) (Miltenyi Biotech,
489 130-092-628) following the manufacturer's protocol with the exception that gentle
490 agitations were performed manually with a P1000 pipette and all incubations were
491 performed at 10°C. Cells were filtered through 70μm cell strainers (SP Bel-Art,
492 136800070), rinsed with ice cold 1x PBS and counted before proceeding with the 10x
493 Chromium Next Single Cell 3' v3.1 platform (single cell preparation, single cell isolation
494 and barcoding performed according to the manufacturer's instructions). Libraries were
495 sequenced (Illumina NovaSeq 6000 S4 flowcell, the DNA services laboratory of the Roy
496 J. Carver Biotechnology Center at the University of Illinois at Urbana-Champaign)
497 followed by quality control (adaptor trimming, de-duplication), alignment and
498 demultiplexing based on manufactured indices using Partek Flow software (Partek Inc.
499 St. Louis, MO, USA, CellRanger).
500
501 *Bioinformatics – single cell RNA sequencing dataset analysis*
502 Analysis of the d1-4 time-course amnion scRNA-seq dataset was performed using the
503 Seurat R package (v.4.2.1, (Hao et al., 2021)). For quality control, cells were filtered out

504 if the total number of detected genes was less than 1,500, if the expression percentage
505 from mitochondrial genes was less than 3% or greater than 15%, or if the total number
506 of transcripts was greater than 30,000. Expression values were then log-normalized
507 with scaling factor 10,000 for cell-level normalization, and further centered and scaled
508 across genes. Principal component analysis (PCA) was performed prior to embedding
509 8,765 cells into two-dimensional space with UMAP using top 15 PCs. Cell clusters were
510 identified using FindNeighbors and FindClusters functions based on a shared nearest
511 neighbor modularity optimization clustering algorithm (resolution set as 0.2). In addition,
512 the "early progenitor" cluster was identified within the original "progenitor" cluster
513 (containing both early and later progenitors) by a gating strategy that sets a cut-off
514 based on the normalized expression levels of TBXT (more than 0.4) and CLDN10 (less
515 than 3.8). Nearby $TBXT^-$ cells within the $TBXT^+$ domain were also included in the "early
516 progenitor" cluster using CellSelector function because those cells are likely due to
517 dropouts. The cluster marker genes were identified using FindAllMarkers function
518 (Wilcoxon Rank Sum test) with adjusted p values less than 0.05.
519
520 *Mapping and gene expression analyses of Tyser et al. Carnegie Stage 7 human embryo*
521 *single cell RNA sequencing dataset*
522 The original UMAP coordinates and annotations for all 1,195 cells were used in **Fig.**
523 **S1C** as well as in the accompanying expression plots. The processed data were
524 downloaded from http://www.human-gastrula.net, which was used to generate a UMAP
525 plot (using DimPlot function in R package Seurat), as well as to perform expression
526 analyses (FeaturePlot function in Seurat).

527

528 *Integration and gene expression analyses of the d1-4 amnion and Tyser et al. Carnegie*
529 *Stage 7 human embryo single cell RNA sequencing datasets*
530 The two single cell datasets were integrated using a canonical correlation analysis
531 based approach implemented in the IntegrateData function with 4,000 anchor features
532 and 50 dimensions for anchor weighting in Seurat R package (v4.2.1).
533

534 *Integration and gene expression analyses of Yang et al. GD14 cynomolgus macaque*
535 *embryo single cell RNA sequencing dataset*
536 The processed data were downloaded from GSE148683, and the ensemble genome
537 build Macaca_fascicularis_5.0 release 96 was used to identify human orthogonal gene
538 symbols. Datasets from two distinct GD14 embryos (Yang et al., 2021) were integrated
539 using 5,000 anchor features and 10 dimensions in the IntegrateData function in Seurat
540 R package (v.4.2.1) package: trophoblast cells were removed from the dataset prior to
541 integration. Six general cell populations (epiblast, transition, mesoderm, amnion,
542 endoderm and extraembryonic mesenchyme) were identified using FindClusters
543 function (resolution as 0.4).
544

545 *RNA velocity (scvelo) analysis*
546 From the aligned BAM files, a loom file was generated for each d1-d4 dataset
547 respectively using the function run10x mode in software velocyto (v0.17) with default
548 parameters to create count matrices made of spliced and unspliced read counts (with
549 Human genome annotation hg19). scVelo (Python package v.0.2.5 (Bergen et al., 2020)

550 was then used to analyze the loom files and examine RNA velocity. Inferred RNA
551 velocity was overlaid onto the UMAP embedding (created by Seurat pipeline as
552 described above) and visualized by stream plot (with default parameters except
553 smoothness was set to 1).
554

555 **FIGURES AND FIGURE LEGENDS**

556 **Figure 1. Single-cell transcriptomic signatures of developing Gel-3D human**
557 **amnion model**

558 (A) Confocal images of d1, d2, d3 and d4 hPSC-amnion cysts stained for TFAP2A, an
559 amnion marker, NANOG, a pluripotency marker, as well as for DNA (blue) and
560 membrane (magenta, using wheat germ agglutinin). White arrowheads indicate cells
561 that display weak TFAP2A expression. Scale bars = 20μm.
562 (B) Quantitation for nuclear aspect ratio, a measure of epithelial cell morphology, of
563 developing hPSC-amnion at indicated timepoints, revealing a gradual squamous
564 morphogenesis (quantitation method in **Fig. S1A**). * indicates $p < 0.05$.
565 (C,D) A UMAP plot displaying the single cell transcriptomes of 1,359 d1 (salmon), 1,546
566 d2 (sage), 2,352 d3 (light blue) and 3,508 d4 Gel-3D cells (C) with seven identified cell
567 populations (D, pluripotency-exiting (salmon, 1,363 cells), early progenitor (brown, 479
568 cells), late progenitor (sage, 1,045 cells), specified (green, 1,366 cells) and maturing
569 (purple, 2,795 cells), PGC-LC (primordial germ cell-like cells, blue, 1,055 cells) and
570 advM-LC (advanced mesoderm-like cells, magenta, 662)).

571 (E-G) Expression of known early (E, *ID2*, *GATA3*, *TFAP2A*), specified (F, *ISL1*, *HAND1*,
572 *DLX5*) and late (G, *GABRP*, *VTCN1*, *IGFBP3*) amnion markers superimposed onto the
573 UMAP plot.
574 (H) RNA velocity analysis of the time-course Gel-3D dataset, showing predicted lineage
575 progression trajectories.
576 (I-K) A UMAP plot showing the integrated single cell transcriptomes of d1-d4 Gel-3D
577 and Tyser *et al.* CS7 embryo datasets, revealing close overlap of Gel-3D amnion
578 progressing cells with Tyser Epiblast, Primitive Streak and Ectoderm/Amnion cells
579 (shown in (I) with original sample, (J) with Gel-3D, and (K) with Tyser *et al.* annotations
580 (individual Tyser annotations plotted in **Fig. S1F**)).
581 (L,M) Expression of primordial germ cell (L, *PRDM1*, *SOX17*, *NANOS3*) and advanced
582 mesoderm (M, *HAND2*, *GATA4*, *PITX2*) markers.
583 (N) Summary of marker expression.
584
585 **Figure 2. Transient expression of TBXT and CLDN10 marks amnion progenitor**
586 **populations**
587 (A,B) Expression of *TBXT* (A) and *CLDN10* (B) superimposed onto the time-course Gel-
588 3D UMAP plot.
589 (C) Expression summary of top three most differentially expressed genes in early
590 progenitor and late progenitor populations.
591 (D,E) Confocal micrographs of developing hPSC-amnion harvested at indicated
592 timepoints, stained with indicated markers. (D) Weak TBXT expression is present at d2
593 (white arrowheads), but is diminished by d3. (E) A white arrowhead indicates a

594 CLDN10/TFAP2A double-positive cell. CLDN10 expression is extinguished by d4.
595 Membrane was stained using wheat germ agglutinin. Scale bars = 20μm
596 (F) Quantitation of CLDN10 expressing cells per cyst in Gel-3D overtime (n = 25 cysts
597 per timepoint).
598
599 **Figure 3. CLDN10 is expressed in amnion progenitor cells at the amnion-epiblast**
600 **boundary of the PASE model as well as cynomolgus macaque peri-gastrula**
601 (A) Optical sections of PASE stained with indicated markers. White arrowheads indicate
602 CLDN10 staining at the amnion-epiblast boundary. Weak CLDN10 signal in the
603 pluripotent territory is likely due to weak CLDN10 expression in the pluripotent cells;
604 brighter signal in the pluripotent territory is likely caused by the boundary cell
605 extensions.
606 (B) Confocal images of a cynomolgus macaque embryo staged at CS6/7 stained using
607 indicated markers. CLDN10 is expressed at the transitioning boundary cells between
608 the amnion and the epiblast. Insets indicate magnified regions.
609 (C,D) Confocal images of cynomolgus macaque embryos staged at CS10 stained using
610 indicated markers. Insets indicate magnified regions. In the CS10 embryo (early
611 organogenesis stage), while some posterior boundary CLDN10 staining is seen (seen in
612 (iii)), the anterior CLDN10 staining is highly prominent at the amnion-anterior surface
613 ectoderm border (in (i)). CLDN10 is also enriched in the dorsal foregut labeled by ISL1/2
614 and SOX2 but not SOX17 (indicated by * in (ii)). **Fig. S3F** provides a bird's-eye view of
615 the CS10 embryo. HT, heat tube; FB, forebrain; YS, yolk sac. White arrowheads
616 indicate the foregut pocket, while white arrows indicate the hindgut pocket.

617 Scale bars = 20μm (A), 200μm (B), 500μm (C,D).

618

619 **Figure 4. CLDN10 is critical for maintaining amnion fate progression in the**

620 **progenitor population.**

621 (A-D) Confocal images of control (A,C) and *CLDN10*-KO (B,D) hPSC grown in Gel-3D,

622 harvested at indicated timepoints and stained with indicated markers. CLDN10

623 expression is not seen in the KO (B). In the absence of *CLDN10*, PGC-LC formation is

624 seen early in d2 cysts, and cyst organization is disrupted by d4. Scale bars = 50μm.

625 (E) Flow chart outlining five continuous amniogenic lineage progressing states with

626 representative markers.

627 (F) A schematic representation of primate peri-gastrula near the primitive streak

628 (generated based on images in **Fig. 3B**, purple cells indicate primitive streak-derived

629 disseminating cells). Transcriptional signatures consistent with amniotic lineage

630 progression (indicated by dotted arrow) are observed at the amnion-epiblast boundary:

631 progressing from SOX2^{+} epiblast cells (blue), CLDN10^{+} transitioning boundary cells

632 (green), and, then, to ISL1^{+} lineage specified amnion (orange).

633

634 **Figure S1. Related to Figure 1**

635 (A) Confocal images of hPSC-amnion stained with indicated markers, outlining nuclear

636 aspect ratio quantitation.

637 (B) Expression of pluripotency markers, SOX2, NANOG and POU5F1, superimposed

638 onto the Gel-3D UMAP plot.

639 (C) A UMAP plot displaying the original single cell transcriptome coordinates of the CS7
640 human embryo described in Tyser *et al.*, shown with the original annotations.
641 (D,E) Expression of indicated broad (D) and late (E) amnion markers superimposed
642 onto the Tyser UMAP plot.
643 (F) UMAP plots showing the integrated single cell transcriptomes of d1-d4 Gel-3D and
644 Tyser *et al.* CS7 embryo datasets with individual Tyser annotations.
645
646 **Figure S2. Validation of selected specified and maturing markers in a cynomolgus**
647 **macaque embryo staged between CS12 and CS13**
648 (A,B) CS12/13 cynomolgus macaque embryo sections were stained for indicated
649 markers (A: *GABRP* – green, *SESN3* – red, *ISL1* – magenta; B: *ADAMTS18* – green,
650 *SESN3* – red, *ISL1* – magenta) using RNA *in situ* hybridization. (i) – (vii) indicate insets:
651 individual channels are shown in gray scale to aid visualization (from left to right:
652 *GABRP*, *SESN3*, *ISL1* and merge in (A), *ADAMTS18*, *SESN3*, *ISL1* in (B)), and dotted
653 lines indicate a layer of amniotic epithelium and mesenchyme. Most amnion cells are
654 positive for *GABRP*, *SESN3* and *ISL1*. *ADAMTS18* expression is restricted to a fraction
655 of cells. In (iv), there are four *ADAMTS18*^{high} cells, while *ADAMTS18* is largely
656 undetected in the amnion in (v). In (vi) and (vii), most cells are *ADAMTS18*^{high}.
657 FB; forebrain, HB, hindbrain; FG, foregut; C; cardiac tissue; NT, neural tube; S, somite.
658 * indicates an *ISL1*$^{+}$ tissue that is likely of genital tubercle lineage. Scale bars = 500μm.
659 (C) An overview image of the CS12/13 embryo implantation site shown in (A). Only
660 nuclear staining is shown in grayscale. Scale bar = 2mm.
661

662 **Figure S3. Additional expression analyses**

663 (A) Expression of *TBXT* and *CLDN10* superimposed onto the uncropped Tyser *et al.*
664 CS7 human embryo UMAP plot.

665 (B) A UMAP plot displaying the GD14 cynomolgus macaque single cell transcriptome
666 with six identified general clusters (epiblast – light blue; transition – purple; amnion –
667 gold; mesoderm – green; endoderm – teal; extraembryonic mesoderm – salmon). Arrow
668 indicates the likely trajectory of amnion differentiation based on the data in Yang *et al.*
669 as well as the expression analysis in (C). Note that, although not identical to the
670 published UMAP plot in Yang *et al.*, general characteristics are well recapitulated.
671 Trophectoderm cells have been omitted as performed in Yang *et al.*.

672 (C) Expression of indicated markers superimposed onto the Yang *et al.* UMAP plot. Late
673 amnion markers (EPAS1 and GABRP) are expressed at the tip of the TFAP2A and ISL1
674 double-positive amnion cluster. CLDN10 positive cells show a weak TBXT expression
675 level.

676 (D,E) Individual channels of the whole embryo images in **Fig. 3C** and **3D**, respectively.

677 (F) An overview image of the CS10 (**Fig. 3C**) embryo implantation sites (DNA signal
678 shown in gray scale, Scale bar = 2mm).

679

680 **Figure S4. Validation of two distinct *CLDN10*-KO hPSC lines**

681 (A) Sequenced genotyping results of *CLDN10*-KO #1 and #2 lines. KO lines #1 and #2
682 have similar phenotype, both displaying an increased formation of PGC-LC and
683 defective cyst organization. The second coding sequence of *CLDN10* was targeted.

684 (B) Representative sequence traces for each mutations.

685

686 **Table 1. Lists of differentially expressed genes in pluripotency-exiting (1506),**
687 **early progenitor (692), late progenitor (697), specified (944), maturing (868), PGC-**
688 **LC (1181) and advM-LC (746) clusters**

689

690 **Table 2. List of antibodies, RNAscope probes, primers and plasmids used in this**
691 **study**

692

693 **ACKNOWLEDGEMENTS**

694 We thank the Wisconsin National Primate Research Center (WNPRC) Veterinary,
695 Scientific Protocol Implementation, Pathology and Animal Services staff for providing
696 animal care, and assisting in procedures including breeding, pregnancy monitoring, and
697 sample collection. A special thanks to Michele Schotzko, Sara Shaw and Drs. Heather
698 Simmons and Puja Basu for their help in generating the macaque specimens. The
699 contents of this manuscript are solely the responsibility of the authors and do not
700 represent the official views of the NIH. We thank Dr. Deborah Gumucio for insightful
701 comments to the manuscript, as well as the Roy J. Carver Biotechnology Center at the
702 University of Illinois at Urbana-Champaign for sequence services.

703

704 **Funding:** This work was supported by NIH grants R01-HD098231 (K.T.), P51
705 OD011106 (to the WNPRC) as well as by MCW CBNA Start-up funds, Advancing a
706 Healthier Wisconsin (AHW) Endowment (16003-5520766, N.S.) and the Lalor
707 Foundation Postdoctoral Fellowship (N.S.). Specifically, MCW CBNA Start-up funds

708 were used to perform experiments using PASE. **Competing interests:** The authors
709 declare no competing interest. **Data and materials availability**: All data needed to
710 evaluate the conclusions in the paper are present in the paper and the Supplementary
711 Materials. The raw data, unfiltered count matrix and processed count matrix will be
712 available to the database of Genotypes and Phenotypes (dbGaP) upon publication.
713 Further information and requests for reagents may be directed to Kenichiro Taniguchi.
714

715 **REFERENCES**

716 Angelow, S., Ahlstrom, R., and Yu, A.S. (2008). Biology of claudins. Am J Physiol Renal
717 Physiol *295*, F867-876.
718 Bergen, V., Lange, M., Peidli, S., Wolf, F.A., and Theis, F.J. (2020). Generalizing RNA
719 velocity to transient cell states through dynamical modeling. Nature biotechnology *38*,
720 1408-1414.
721 Bergmann, S., Penfold, C.A., Slatery, E., Siriwardena, D., Drummer, C., Clark, S.,
722 Strawbridge, S.E., Kishimoto, K., Vickers, A., Tewary, M.*, et al.* (2022). Spatial profiling
723 of early primate gastrulation in utero. Nature *609*, 136-143.
724 Butler, A., Hoffman, P., Smibert, P., Papalexi, E., and Satija, R. (2018). Integrating
725 single-cell transcriptomic data across different conditions, technologies, and species.
726 Nature biotechnology *36*, 411-420.
727 Carleton, A.E., Duncan, M.C., and Taniguchi, K. (2022). Human epiblast
728 lumenogenesis: From a cell aggregate to a lumenal cyst. Seminars in cell &
729 developmental biology *131*, 117-123.
730 Castillo-Venzor, A., Penfold, C.A., Morgan, M.D., Tang, W.W., Kobayashi, T., Wong,
731 F.C., Bergmann, S., Slatery, E., Boroviak, T.E., Marioni, J.C.*, et al.* (2023). Origin and
732 segregation of the human germline. Life Sci Alliance *6*.
733 Chambers, S.M., Fasano, C.A., Papapetrou, E.P., Tomishima, M., Sadelain, M., and
734 Studer, L. (2009). Highly efficient neural conversion of human ES and iPS cells by dual
735 inhibition of SMAD signaling. Nature biotechnology *27*, 275-280.
736 Chen, D., Sun, N., Hou, L., Kim, R., Faith, J., Aslanyan, M., Tao, Y., Zheng, Y., Fu, J.,
737 Liu, W.*, et al.* (2019). Human Primordial Germ Cells Are Specified from Lineage-Primed
738 Progenitors. Cell reports *29*, 4568-4582 e4565.
739 Chen, F., and LoTurco, J. (2012). A method for stable transgenesis of radial glia lineage
740 in rat neocortex by piggyBac mediated transposition. Journal of neuroscience methods
741 *207*, 172-180.
742 Chen, K., Zheng, Y., Xue, X., Liu, Y., Resto Irizarry, A.M., Tang, H., and Fu, J. (2021).
743 Branching development of early post-implantation human embryonic-like tissues in 3D
744 stem cell culture. Biomaterials *275*, 120898.

745 Enders, A.C., Hendrickx, A.G., and Schlafke, S. (1983). Implantation in the rhesus
746 monkey: initial penetration of endometrium. The American journal of anatomy *167*, 275-
747 298.
748 Enders, A.C., Schlafke, S., and Hendrickx, A.G. (1986). Differentiation of the embryonic
749 disc, amnion, and yolk sac in the rhesus monkey. The American journal of anatomy
750 *177*, 161-185.
751 Hamed, M.M., Taniguchi, K., and Duncan, M.C. (2023). Monitoring Effects of Membrane
752 Traffic Via Changes in Cell Polarity and Morphogenesis in Three-Dimensional Human
753 Pluripotent Stem Cell Cysts. Methods in molecular biology *2557*, 83-98.
754 Hao, Y., Hao, S., Andersen-Nissen, E., Mauck, W.M., 3rd, Zheng, S., Butler, A., Lee,
755 M.J., Wilk, A.J., Darby, C., Zager, M.*, et al.* (2021). Integrated analysis of multimodal
756 single-cell data. Cell *184*, 3573-3587 e3529.
757 Heemskerk, I., Burt, K., Miller, M., Chhabra, S., Guerra, M.C., and Warmflash, A.
758 (2017). Morphogen dynamics control patterning in a stem cell model of human embryo.
759 bioRxiv *http://dx.doi.org/10.1101/202366*.
760 Joy, D.A., Libby, A.R.G., and McDevitt, T.C. (2021). Deep neural net tracking of human
761 pluripotent stem cells reveals intrinsic behaviors directing morphogenesis. Stem cell
762 reports *16*, 1317-1330.
763 Lacoste, A., Berenshteyn, F., and Brivanlou, A.H. (2009). An efficient and reversible
764 transposable system for gene delivery and lineage-specific differentiation in human
765 embryonic stem cells. Cell stem cell *5*, 332-342.
766 Miki, T., Lehmann, T., Cai, H., Stolz, D.B., and Strom, S.C. (2005). Stem cell
767 characteristics of amniotic epithelial cells. Stem cells *23*, 1549-1559.
768 Minn, K.T., Fu, Y.C., He, S., Dietmann, S., George, S.C., Anastasio, M.A., Morris, S.A.,
769 and Solnica-Krezel, L. (2020). High-resolution transcriptional and morphogenetic
770 profiling of cells from micropatterned human ESC gastruloid cultures. eLife *9*.
771 Nakamura, T., Okamoto, I., Sasaki, K., Yabuta, Y., Iwatani, C., Tsuchiya, H., Seita, Y.,
772 Nakamura, S., Yamamoto, T., and Saitou, M. (2016). A developmental coordinate of
773 pluripotency among mice, monkeys and humans. Nature *537*, 57-62.
774 Nakamura, T., Yabuta, Y., Okamoto, I., Sasaki, K., Iwatani, C., Tsuchiya, H., and
775 Saitou, M. (2017). Single-cell transcriptome of early embryos and cultured embryonic
776 stem cells of cynomolgus monkeys. Scientific data *4*, 170067.
777 Overeem, A.W., Chang, Y.W., Moustakas, I., Roelse, C.M., Hillenius, S., Helm, T.V.,
778 Schrier, V.F.V., Goncalves, M., Mei, H., Freund, C.*, et al.* (2023). Efficient and scalable
779 generation of primordial germ cells in 2D culture using basement membrane extract
780 overlay. Cell Rep Methods *3*, 100488.
781 Pedroza, M., Gassaloglu, S.I., Dias, N., Zhong, L., Hou, T.J., Kretzmer, H., Smith, Z.D.,
782 and Sozen, B. (2023). Self-patterning of human stem cells into post-implantation
783 lineages. Nature *622*, 574-583.
784 Perea-Gomez, A., Vella, F.D., Shawlot, W., Oulad-Abdelghani, M., Chazaud, C., Meno,
785 C., Pfister, V., Chen, L., Robertson, E., Hamada, H.*, et al.* (2002). Nodal antagonists in
786 the anterior visceral endoderm prevent the formation of multiple primitive streaks.
787 Developmental cell *3*, 745-756.
788 Roost, M.S., van Iperen, L., Ariyurek, Y., Buermans, H.P., Arindrarto, W., Devalla, H.D.,
789 Passier, R., Mummery, C.L., Carlotti, F., de Koning, E.J.*, et al.* (2015). KeyGenes, a

Tool to Probe Tissue Differentiation Using a Human Fetal Transcriptional Atlas. Stem cell reports *4*, 1112-1124.
Rostovskaya, M., Andrews, S., Reik, W., and Rugg-Gunn, P.J. (2022). Amniogenesis occurs in two independent waves in primates. Cell stem cell *29*, 744-759 e746.
Sasaki, K., Nakamura, T., Okamoto, I., Yabuta, Y., Iwatani, C., Tsuchiya, H., Seita, Y., Nakamura, S., Shiraki, N., Takakuwa, T.*, et al.* (2016). The Germ Cell Fate of Cynomolgus Monkeys Is Specified in the Nascent Amnion. Developmental cell *39*, 169-185.
Schultheiss, T.M., Burch, J.B., and Lassar, A.B. (1997). A role for bone morphogenetic proteins in the induction of cardiac myogenesis. Genes & development *11*, 451-462.
Sekulovski, N., Wettstein, J.C., Carleton, A.E., Juga, L.N., Taniguchi, L.E., Ma, X., Rao, S., Schmidt, J.K., Golos, T.G., Lin, C.W.*, et al.* (2024). Temporally resolved early bone morphogenetic protein-driven transcriptional cascade during human amnion specification. eLife *12*.
Shahbazi, M.N., and Zernicka-Goetz, M. (2018). Deconstructing and reconstructing the mouse and human early embryo. Nature cell biology.
Shao, Y., and Fu, J. (2022). Engineering multiscale structural orders for high-fidelity embryoids and organoids. Cell stem cell *29*, 722-743.
Shao, Y., Taniguchi, K., Gurdziel, K., Townshend, R.F., Xue, X., Yong, K.M.A., Sang, J., Spence, J.R., Gumucio, D.L., and Fu, J. (2017a). Self-organized amniogenesis by human pluripotent stem cells in a biomimetic implantation-like niche. Nature materials *16*, 419-425.
Shao, Y., Taniguchi, K., Townshend, R.F., Miki, T., Gumucio, D.L., and Fu, J. (2017b). A pluripotent stem cell-based model for post-implantation human amniotic sac development. Nature communications *8*, 208.
Shawlot, W., Wakamiya, M., Kwan, K.M., Kania, A., Jessell, T.M., and Behringer, R.R. (1999). Lim1 is required in both primitive streak-derived tissues and visceral endoderm for head formation in the mouse. Development *126*, 4925-4932.
Taniguchi, K., Heemskerk, I., and Gumucio, D.L. (2019). Opening the black box: Stem cell-based modeling of human post-implantation development. The Journal of cell biology *218*, 410-421.
Taniguchi, K., Shao, Y., Townshend, R.F., Tsai, Y.H., DeLong, C.J., Lopez, S.A., Gayen, S., Freddo, A.M., Chue, D.J., Thomas, D.J.*, et al.* (2015). Lumen Formation Is an Intrinsic Property of Isolated Human Pluripotent Stem Cells. Stem cell reports *5*, 954-962.
Townshend, R.F., Shao, Y., Wang, S., Cortez, C.L., Esfahani, S.N., Spence, J.R., O'Shea, K.S., Fu, J., Gumucio, D.L., and Taniguchi, K. (2020). Effect of Cell Spreading on Rosette Formation by Human Pluripotent Stem Cell-Derived Neural Progenitor Cells. Front Cell Dev Biol *8*, 588941.
Tsaytler, P., Liu, J., Blaess, G., Schifferl, D., Veenvliet, J.V., Wittler, L., Timmermann, B., Herrmann, B.G., and Koch, F. (2023). BMP4 triggers regulatory circuits specifying the cardiac mesoderm lineage. Development *150*.
Tyser, R.C.V., Mahammadov, E., Nakanoh, S., Vallier, L., Scialdone, A., and Srinivas, S. (2021). Single-cell transcriptomic characterization of a gastrulating human embryo. Nature *600*, 285-289.

van Wijk, B., Moorman, A.F., and van den Hoff, M.J. (2007). Role of bone morphogenetic proteins in cardiac differentiation. Cardiovasc Res *74*, 244-255.

Vasic, I., Libby, A.R.G., Maslan, A., Bulger, E.A., Zalazar, D., Krakora Compagno, M.Z., Streets, A., Tomoda, K., Yamanaka, S., and McDevitt, T.C. (2023). Loss of TJP1 disrupts gastrulation patterning and increases differentiation toward the germ cell lineage in human pluripotent stem cells. Developmental cell *58*, 1477-1488 e1475.

Wang, S., Lin, C.W., Carleton, A.E., Cortez, C.L., Johnson, C., Taniguchi, L.E., Sekulovski, N., Townshend, R.F., Basrur, V., Nesvizhskii, A.I.*, et al.* (2021). Spatially resolved cell polarity proteomics of a human epiblast model. Sci Adv *7*.

Warmflash, A., Sorre, B., Etoc, F., Siggia, E.D., and Brivanlou, A.H. (2014). A method to recapitulate early embryonic spatial patterning in human embryonic stem cells. Nature methods *11*, 847-854.

Xiao, Z., Cui, L., Yuan, Y., He, N., Xie, X., Lin, S., Yang, X., Zhang, X., Shi, P., Wei, Z.*, et al.* (2024). 3D reconstruction of a gastrulating human embryo. Cell *187*, 2855-2874 e2819.

Yang, R., Goedel, A., Kang, Y., Si, C., Chu, C., Zheng, Y., Chen, Z., Gruber, P.J., Xiao, Y., Zhou, C.*, et al.* (2021). Amnion signals are essential for mesoderm formation in primates. Nature communications *12*, 5126.

Zhao, C., Plaza Reyes, A., Schell, J.P., Weltner, J., Ortega, N.M., Zheng, Y., Björklund, Å.K., Baque-Vidal, L., Sokka, J., Torokovic, R.*, et al.* (2024). A comprehensive human embryogenesis reference tool using single-cell RNA sequencing data. bioRxiv *doi: 10.1101/2021.05.07.442980*.

Zheng, Y., Xue, X., Shao, Y., Wang, S., Esfahani, S.N., Li, Z., Muncie, J.M., Lakins, J.N., Weaver, V.M., Gumucio, D.L.*, et al.* (2019). Controlled modelling of human epiblast and amnion development using stem cells. Nature *573*, 421-425.

Zheng, Y., Yan, R.Z., Sun, S., Kobayashi, M., Xiang, L., Yang, R., Goedel, A., Kang, Y., Xue, X., Esfahani, S.N.*, et al.* (2022). Single-cell analysis of embryoids reveals lineage diversification roadmaps of early human development. Cell stem cell *29*, 1402-1419 e1408.

Figure 1

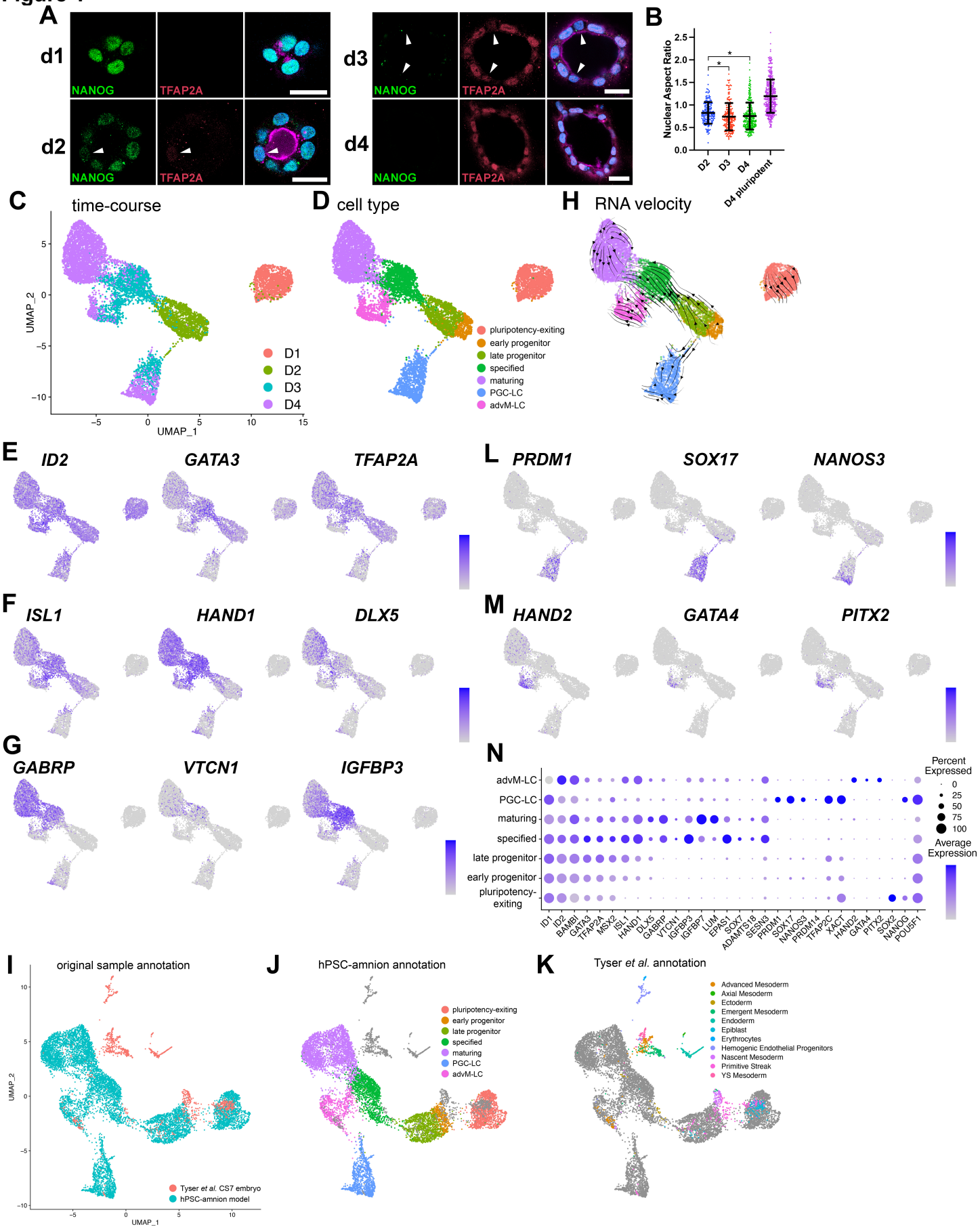
A
d1
d2
d3
d4
NANOG
TFAP2A
B
Nuclear Aspect Ratio
D2
D3
D4
D4 pluripotent
C
time-course
UMAP_1
UMAP_2
D1
D2
D3
D4
D
cell type
pluripotency-exiting
early progenitor
late progenitor
specified
maturing
PGC-LC
advM-LC
H
RNA velocity
E
ID2
GATA3
TFAP2A
L
PRDM1
SOX17
NANOS3
F
ISL1
HAND1
DLX5
M
HAND2
GATA4
PITX2
G
GABRP
VTCN1
IGFBP3
N
advM-LC
PGC-LC
maturing
specified
late progenitor
early progenitor
pluripotency-exiting
ID1
ID2
BAMBI
GATA3
TFAP2A
MSX2
ISL1
HAND1
DLX5
GABRP
VTCN1
IGFBP3
IGFBP7
LUM
EPAS1
SOX7
ADAMTS18
SESN3
PRDM1
SOX17
NANOS3
PRDM14
TFAP2C
XACT
HAND2
GATA4
PITX2
SOX2
NANOG
POU5F1
Percent Expressed
0
25
50
75
100
Average Expression
I
original sample annotation
Tyser et al. CS7 embryo
hPSC-amnion model
J
hPSC-amnion annotation
pluripotency-exiting
early progenitor
late progenitor
specified
maturing
PGC-LC
advM-LC
K
Tyser et al. annotation
Advanced Mesoderm
Axial Mesoderm
Ectoderm
Emergent Mesoderm
Endoderm
Epiblast
Erythrocytes
Hemogenic Endothelial Progenitors
Nascent Mesoderm
Primitive Streak
YS Mesoderm

Figure 2

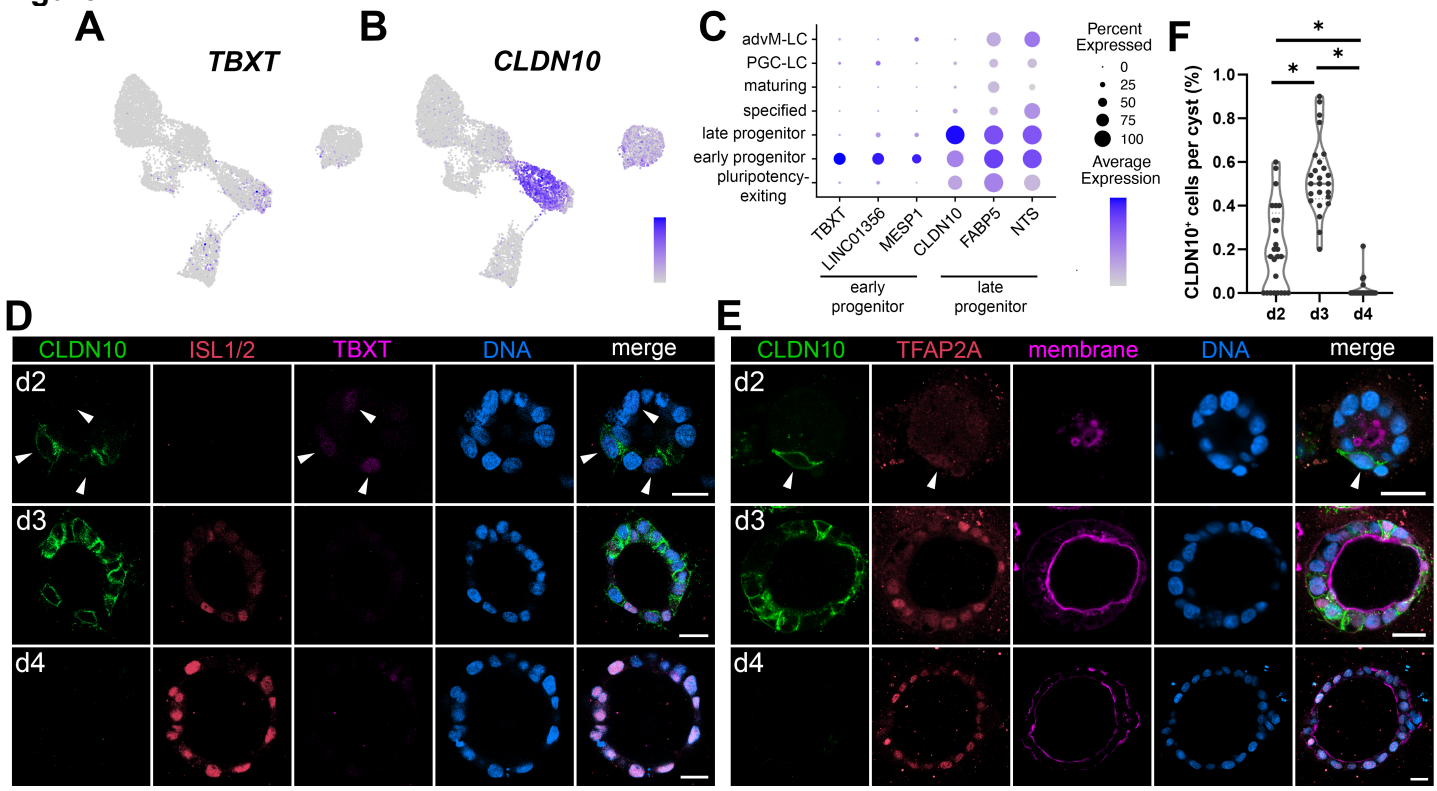
A
TBXT
B
CLDN10
C
advM-LC
PGC-LC
maturing
specified
late progenitor
early progenitor
pluripotency-exiting
TBXT
LINC01356
MESP1
CLDN10
FABP5
NTS
early progenitor
late progenitor
Percent Expressed
0
25
50
75
100
Average Expression
F
CLDN10+ cells per cyst (%)
1.0
0.8
0.6
0.4
0.2
0.0
d2
d3
d4
D
CLDN10
ISL1/2
TBXT
DNA
merge
d2
d3
d4
E
CLDN10
TFAP2A
membrane
DNA
merge
d2
d3
d4

Figure 3

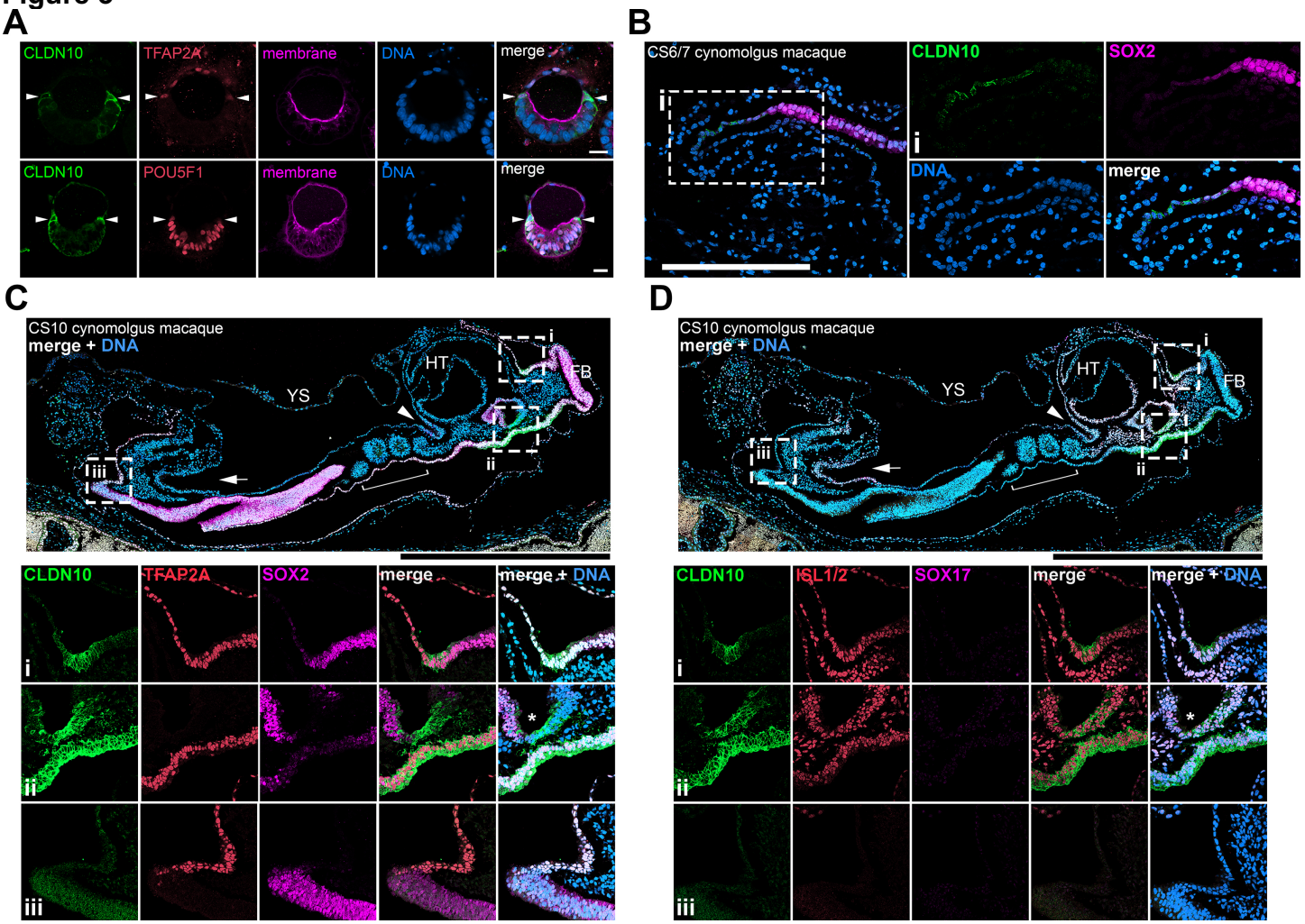
A
CLDN10
TFAP2A
membrane
DNA
merge
CLDN10
POU5F1
membrane
DNA
merge
B
CS6/7 cynomolgus macaque
CLDN10
SOX2
i
DNA
merge
C
CS10 cynomolgus macaque
merge + DNA
YS
HT
FB
i
ii
iii
CLDN10
TFAP2A
SOX2
merge
merge + DNA
*
D
CS10 cynomolgus macaque
merge + DNA
YS
HT
FB
i
ii
iii
CLDN10
ISL1/2
SOX17
merge
merge + DNA
*

Figure 4

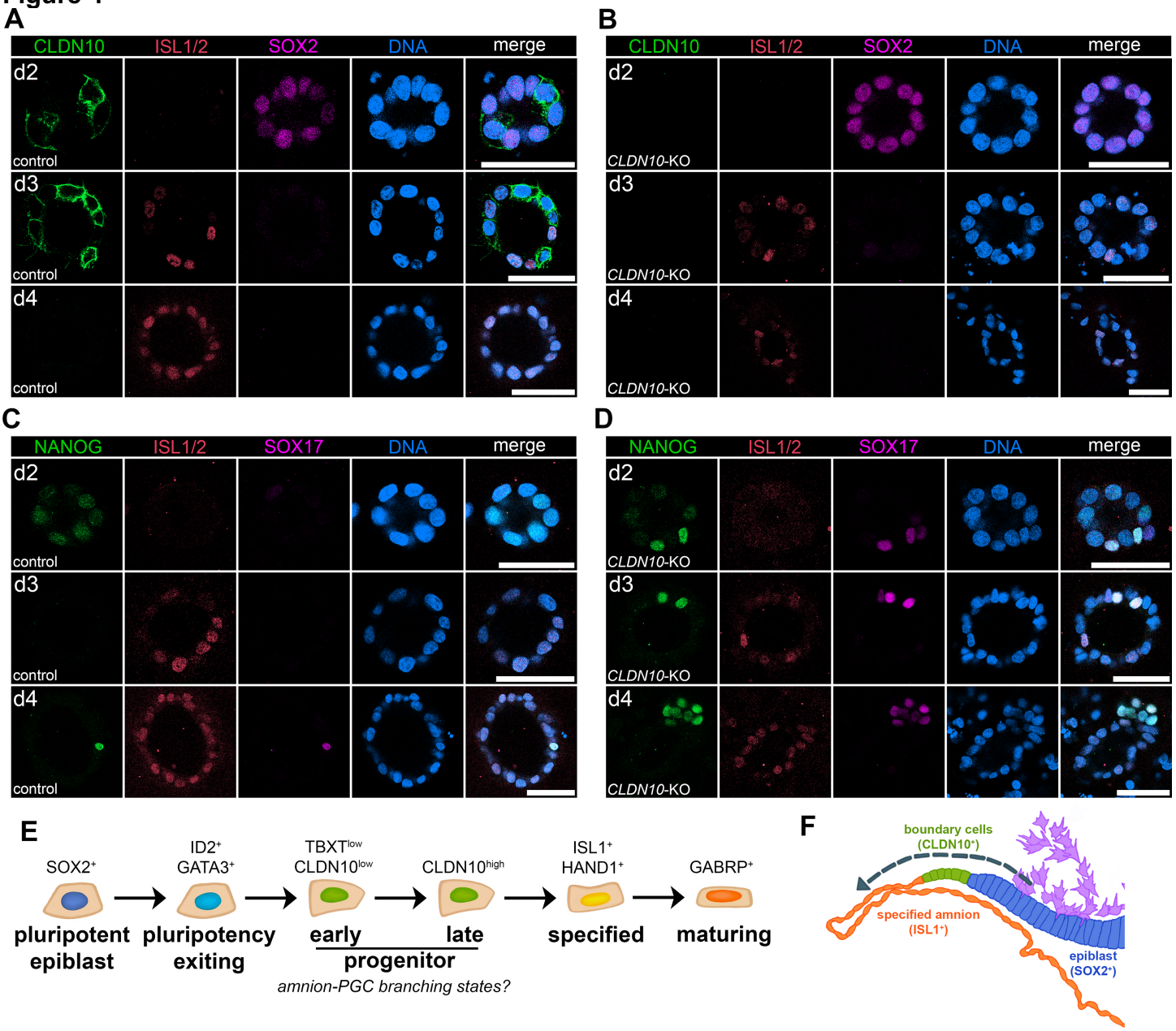
A
CLDN10
ISL1/2
SOX2
DNA
merge
d2
d3
d4
control
B
CLDN10-KO
C
NANOG
SOX17
D
E
SOX2+
pluripotent epiblast
ID2+
GATA3+
pluripotency exiting
TBXTlow
CLDN10low
early
CLDN10high
late
progenitor
ISL1+
HAND1+
specified
GABRP+
maturing
amnion-PGC branching states?
F
boundary cells (CLDN10+)
specified amnion (ISL1+)
epiblast (SOX2+)

Figure S1

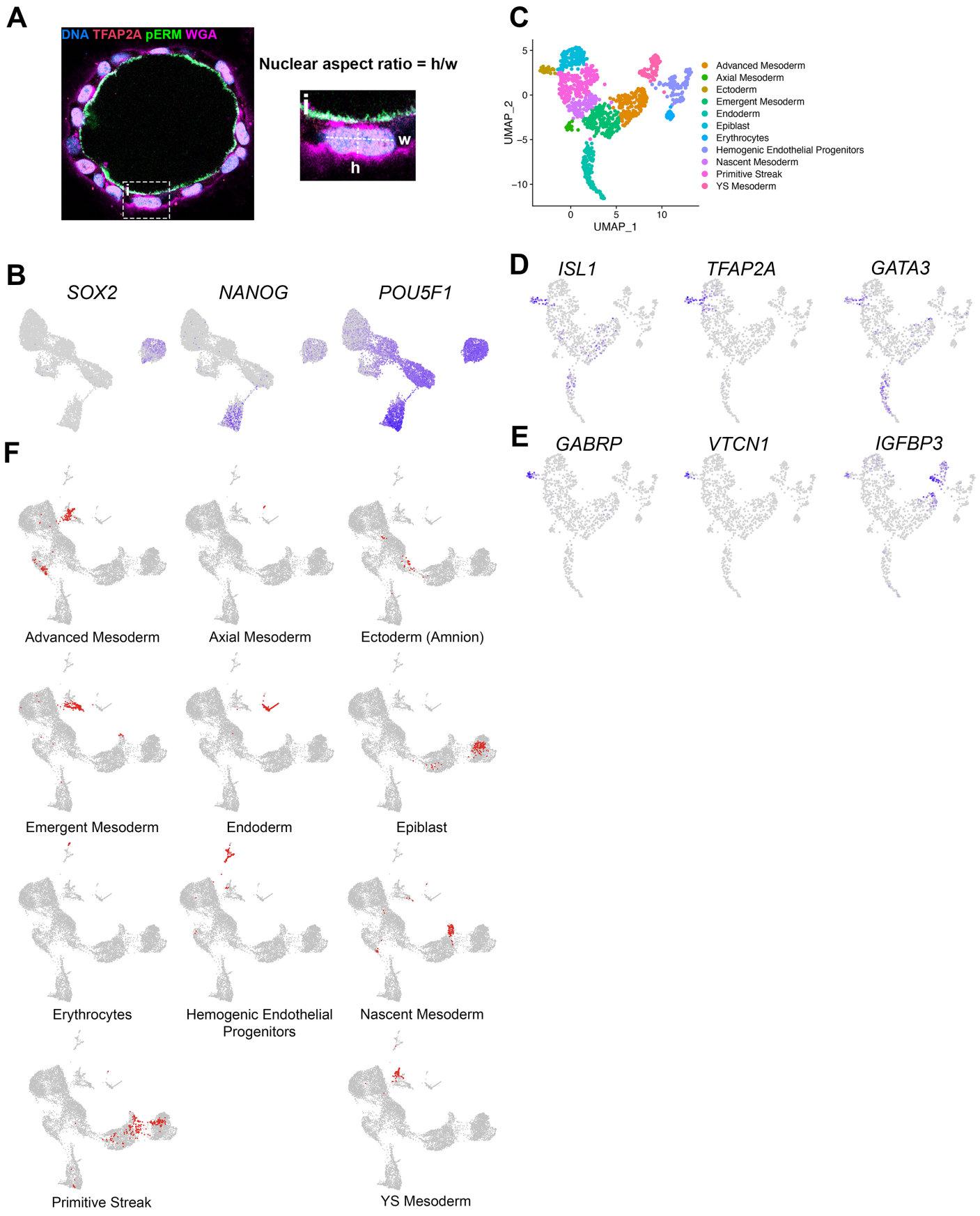
A
DNA TFAP2A pERM WGA
Nuclear aspect ratio = h/w
i
w
h
C
UMAP_2
UMAP_1
Advanced Mesoderm
Axial Mesoderm
Ectoderm
Emergent Mesoderm
Endoderm
Epiblast
Erythrocytes
Hemogenic Endothelial Progenitors
Nascent Mesoderm
Primitive Streak
YS Mesoderm
B
SOX2
NANOG
POU5F1
D
ISL1
TFAP2A
GATA3
E
GABRP
VTCN1
IGFBP3
F
Advanced Mesoderm
Axial Mesoderm
Ectoderm (Amnion)
Emergent Mesoderm
Endoderm
Epiblast
Erythrocytes
Hemogenic Endothelial Progenitors
Nascent Mesoderm
Primitive Streak
YS Mesoderm

Figure S2

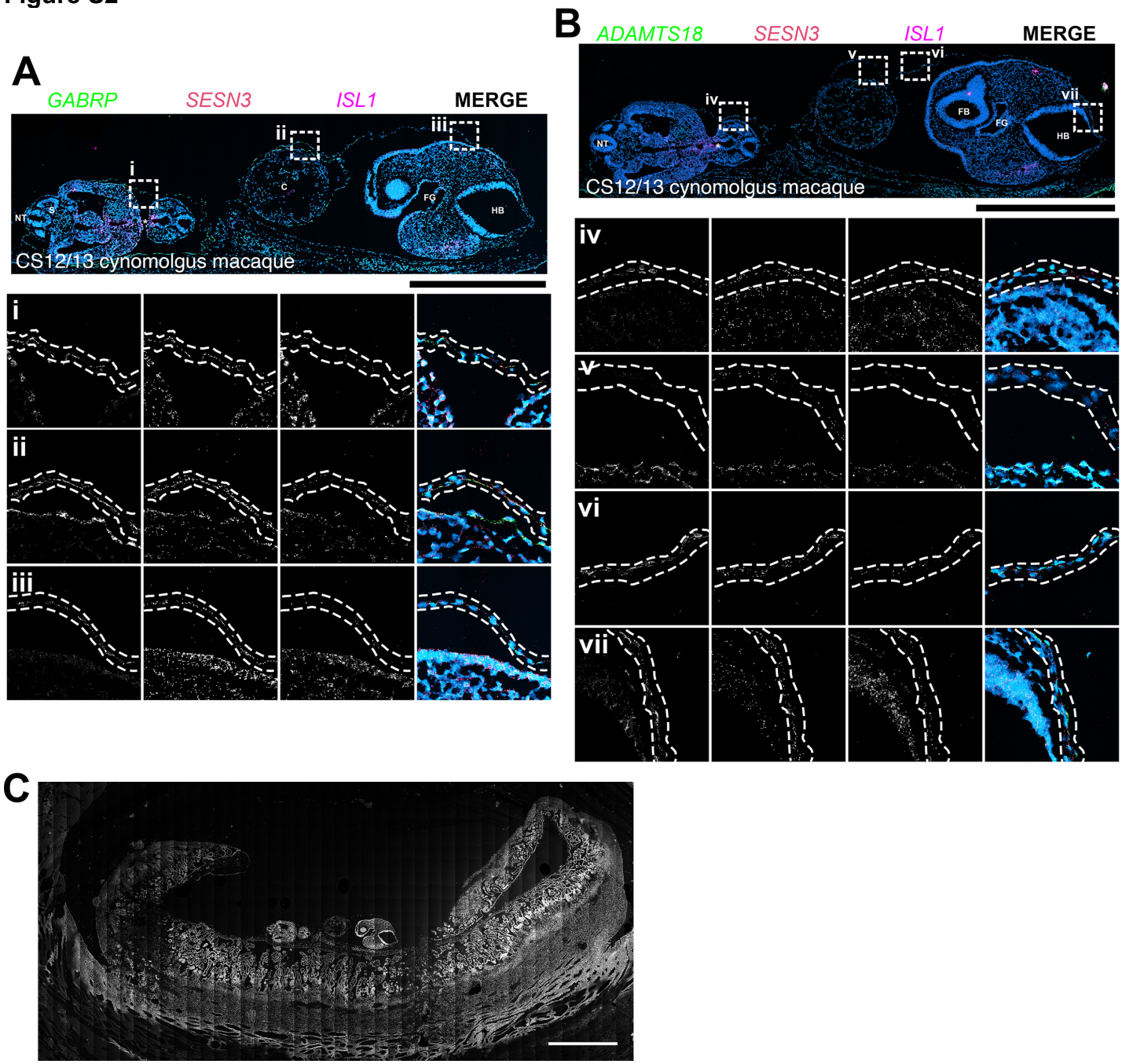
A
GABRP
SESN3
ISL1
MERGE
i
ii
iii
NT
S
C
FG
HB
CS12/13 cynomolgus macaque
B
ADAMTS18
SESN3
ISL1
MERGE
iv
v
vi
vii
NT
FB
FG
HB
CS12/13 cynomolgus macaque
C

Figure S3

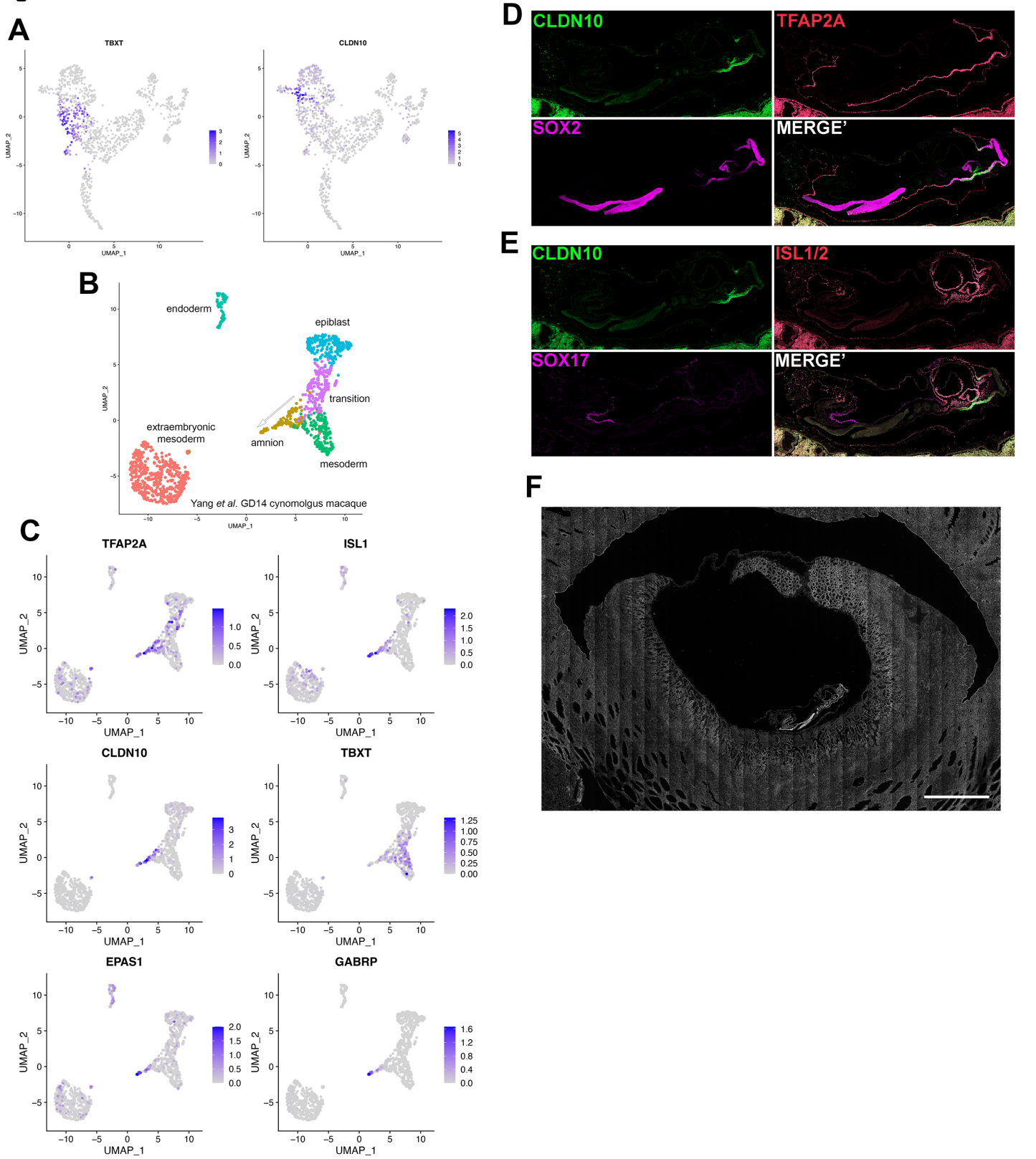
A
TBXT
CLDN10
UMAP_1
UMAP_2
B
endoderm
epiblast
transition
extraembryonic mesoderm
amnion
mesoderm
Yang et al. GD14 cynomolgus macaque
C
TFAP2A
ISL1
CLDN10
TBXT
EPAS1
GABRP
D
CLDN10
TFAP2A
SOX2
MERGE'
E
CLDN10
ISL1/2
SOX17
MERGE'
F

Figure S4

A Green: PAM Red: Target sequence --- : Deletion

CLDN10-WT	1. ATGAAGTGTACCAAAGTCGGAGGCTCCGATAAAGCCAAAGCTAAA	
	2. ATGAAGTGTACCAAAGTCGGAGGCTCCGATAAAGCCAAAGCTAAA	
CLDN10-KO #1	1. ATGAAGTGTAC- - - - - - - - - - - - - TCCGATAAAGCCAAAGCTAAA	(13bp deletion)
	2. ATGAAGTGTACCAAA- -CGGAGGCTCCGATAAAGCCAAAGCTAAA	(2bp deletion)
CLDN10-KO #2	1. ATGAAGTGTACCAAA-TCGGAGGCTCCGATAAAGCCAAAGCTAAA	(1bp deletion)
	2. ATGAAGTGTACCAAA-TCGGAGGCTCCGATAAAGCCAAAGCTAAA	(1bp deletion)

B